Motion-Robust, High-SNR Liver Fat Quantification using a 2D Sequential Acquisition with a Variable Flip Angle Approach

Ruiyang Zhao[1,2], **Yuxin Zhang**[1,2], **Xiaoke Wang**[1,3], **Timothy J. Colgan**[1,2], **Jennifer L. Rehm**[4], **Scott B. Reeder**[1,2,3,5,6], **Kevin M. Johnson**[1,2], **Diego Hernando**[1,2]

[1]Department of Radiology, University of Wisconsin-Madison, Madison, WI, 53705, USA

[2]Department of Medical Physics, University of Wisconsin-Madison, Madison, WI, 53705, USA

[3]Department of Biomedical Engineering, University of Wisconsin-Madison, Madison, WI, 53705, USA

[4]Department of Pediatric, University of Wisconsin-Madison, Madison, WI, 53705, USA

[5]Department of Medicine, University of Wisconsin-Madison, Madison, WI, 53705, USA

[6]Department of Emergency Medicine, University of Wisconsin-Madison, Madison, WI, 53705, USA

Abstract

Purpose: Chemical shift encoded (CSE)-MRI enables quantification of proton density fat fraction (PDFF) as a biomarker of liver fat content. However, conventional 3D Cartesian CSE-MRI methods require breath-holding. A motion-robust 2D Cartesian sequential method addresses this limitation but suffers from low SNR. In this work, a novel free breathing 2D Cartesian sequential CSE-MRI method using a variable flip angle approach with centric phase encoding (VFA-centric) is developed to achieve fat quantification with low T_1 bias, high SNR, and minimal blurring.

Methods: Numerical simulation was performed for variable flip angle schedule design and preliminary evaluation of VFA-centric method, along with several alternative flip angle designs. Phantom, adults (n = 8), and children (n = 27) were imaged at 3T. Multi-echo images were acquired and PDFF maps were estimated. PDFF standard deviation was used as a surrogate for SNR.

Results: In both simulation and phantom experiments, the VFA-centric method enabled higher SNR imaging with minimal T_1 bias and blurring artifacts. High correlation (slope = 1.00, intercept = 0.04, R^2 = 0.998) was observed in vivo between the proposed VFA-centric method obtained PDFF and reference PDFF (free breathing low flip angle 2D sequential acquisition). Further, the proposed VFA-centric method (PDFF standard deviation = 1.5%) had better SNR performance than the reference acquisition (PDFF standard deviation = 3.3%) with p<0.001.

Correspondence Diego Hernando, Department of Radiology, University of Wisconsin-Madison, Madison, WI, 53705, USA, dhernando@wisc.edu.

Conclusion: The proposed free breathing 2D Cartesian sequential CSE-MRI method with variable flip angle approach and centric-ordered phase encoding achieved motion robustness, low T_1 bias, high SNR compared to previous 2D sequential methods, and low blurring in liver fat quantification.

Keywords

Free breathing; Liver fat; 2D Cartesian; Variable flip angle; Low T_1 bias; High SNR; Low blurring artifact

1 | INTRODUCTION

Abnormal intracellular accumulation of trigylcerides within hepatocytes is the hallmark and earliest feature of nonalcoholic fatty liver disease (NAFLD)[1, 2, 3]. NAFLD consists of a continuum from isolated hepatic steatosis (HS) to steatohepatits (NASH) and can progress to fibrosis, and eventually cirrhosis, including the development of portal hypertension, liver failure and hepatocellular carcinoma[1, 2, 3]. Further, hepatic steatosis confers a substantially elevated risk of developing type 2 diabetes[4] and is an independent risk factor for cardiovascular diseases[5, 6, 7, 8]. The prevalence of NAFLD is high in the general population as well as among children, especially overweight children. In the United States, an estimated 15% of children are overweight or obese with excess fat deposition in the liver[9, 10]. Lifestyle interventions (primarily aimed at weight loss) may be effective in NAFLD patients[11]. Given the high prevalence and associated risks, there is an urgent need for non-invasive and accurate liver fat quantifcation, particularly for pediatric patients.

Chemical shift encoded (CSE)-MRI methods for liver fat quantifcation have been developed, validated, and applied in multiple studies. Upon correction for relevant confounding factors, including the presence of R2* relaxation, spectral complexity of fat, and T_1 bias, these methods provide reliable and reproducible mapping of proton-density fat fraction (PDFF), a quantitative MR imaging biomarker of triglyceride concentration (i.e., ratio of MR-visible triglyceride protons to all MR-visible protons). Generally, three-dimensional (3D) CSE-MRI acquisitions obtained in a single 20-second breath-hold are used for liver PDFF mapping[12,13,14,15]. Although these methods are reliable for many patients, substantial image artifacts and unreliable quantifcation are common in patients who are unable to sustain such prolonged breath-holds[16]. Children, elderly, and sick patients may not be capable of sustaining such prolonged breath-holds, resulting in unreliable fat quantifcation using standard 3D CSE-MRI methods.

In order to overcome this challenge, several motion-robust CSE-MRI methods have been proposed. Respiratory-gated 3D Cartesian CSE-MRI methods using respiratory bellows or navigators have demonstrated promising performance for liver fat quantification[17]. However, 3D Cartesian methods generally contain residual motion artifacts, particularly in the presence of irregular breathing. As an alternative, 3D non-Cartesian methods have shown potential to enable motion-robust free breathing (FB) CSE-MRI acquisitions. Specifcally, 3D stack of stars (FB radial) approach has been recently shown to provide reliable PDFF mapping during free breathing with excellent image quality[18]. Despite the promising

performance of non-Cartesian methods, the vast majority of clinical and research CSE-MRI acquisitions are based on Cartesian acquisitions, which are highly robust (across different vendors, different feld strengths, and different acquisitions[27, 40]) and enable simple reconstruction methods.

In order to improve motion robustness with Cartesian acquisitions, rapid single-shot 2D Cartesian sequential CSE-MRI has been recently proposed[19, 16]. This approach dramatically decreases the acquisition time required for each slice (i.e., short temporal footprint on the order of 1 second), which effectively freezes breathing motion. Importantly, this method uses a low flip angle (typically 3°-4° at 3T) to avoid T_1 bias[12, 20] in PDFF measurement. Although effective for avoiding bias, this low flip angle approach leads to severely reduced signal-to-noise ratio (SNR), particularly when compounded with the inherently low SNR of a 2D sequential acquisition. Even through multiple repetitions can be applied to improve SNR[21], these methods extend the scan time and may lead to additional blurring and artifacts. For these reasons, a 2D Cartesian sequential CSE-MRI method with inherently higher SNR compared to current low flip angle methods would be highly desirable.

Therefore, the purpose of this work was to develop a novel free breathing 2D Cartesian sequential CSE-MRI method with low bias and high SNR (i.e., low standard deviation in PDFF measurements compared to previous 2D sequential methods) in fatquantifcation. The proposed approach is based on a centric-ordered phase encoding strategy with variable flip angle design[22, 23, 24, 25]. This method is designed to provide motion-robust, confounder-corrected, high-SNR liver fat quantifcation, appropriate for applications in pediatric imaging.

2 | THEORY

Conventional 3D Cartesian CSE-MRI acquisitions require either breath-holding or respiratory-gating[17] for reliable imaging of the abdomen. Poor breath-holding or irregular breathing patterns result in residual motion artifacts in these 3D CSE-MRI methods. In contrast, rapid 2D Cartesian sequential "single-shot" CSE-MRI acquisitions have a very short temporal footprint (on the order of 1 second per slice) and effectively freeze breathing motion [16]. These 2D sequential acquisitions are typically performed using linear phase encoding (such that the center of k-space is acquired as the signal approaches steady state), and a constant low flip angle (e.g., 3° at 3T) in order to avoid T_1 bias in PDFF mapping.

The major drawback of rapid 2D CSE-MRI with sequential acquisitions, linear phase encoding and low flip angles is low SNR performance. While higher flip angles can be used to enhanced SNR, this leads to T_1 bias in PDFF quantifcation and is therefore avoided by most fat quantifcation methods. This trade-off between SNR and T_1 bias is a fundamental limitation of 2D CSE-MRI methods that use linear phase encoding.

In contrast to linear phase encoding, centric-ordered encoding along the phase encoding direction may enable methods that overcome this limitation. With centric-ordered phase encoding, the acquisition is performed during the transient state magnetization (i.e., not in

steady state equilibrium magnetization). Therefore, more longitudinal magnetization (higher SNR) is available for gradient echo imaging, particularly for the central lines of k-space that are acquired frst. Further, there is no T_1 bias in the frst TR (since both water and fat magnetization start in equilibrium without T_1 weighting). Therefore, centric-ordered phase encoding may enable CSE-MRI imaging with higher SNR and low T_1 bias. However, high flip angles will rapidly drive magnetization to a much lower steady state causing k-space amplitude modulation and blurring in the reconstructed images. As the amplitude modulation is dependent on T_1 which differ for fat and water, magnetization modulations introduce differential blurring for fat and water signals and potentially T_1 bias in PDFF estimation.

In this manuscript, we propose a novel 2D Cartesian CSE-MRI method for fat quantification, based on rapid sequential single-shot 2D CSE-MRI acquisition with a variable flip angle (VFA) approach and centric-ordered phase encoding. Variable flip angle schedules are often used to control magnetization modulations from RF excitation and relaxation as in cardiac tagging[23, 24], hyperpolarized MRI [22], and in imaging with extended spin echo trains[25]. This study proposes a variable flip angle schedule optimized for CSE using the joint consideration of three competing criteria: i) minimize the T_1 bias in PDFF estimation; ii) achieve high SNR by maximizing the measured gradient echo (GRE) signals; iii) preserve the consistency of signals (i.e., water and fat) across k-space and minimize blurring artifacts. Specifically, the design of flip angle schedule in the proposed VFA approach is posed as an optimization problem, formulated as follows:

$$
\vec{\theta} = \underset{\vec{\theta}}{\arg\min}(\sum_i \lambda_1 \cdot \mid S_{fat}(\theta_i) - S_{water}(\theta_i) \mid^2 - \sum_i \lambda_2 \cdot (S_{fat}(\theta_i) + S_{water}(\theta_i))^2
$$
$$
+ \sum_i \lambda_3 \cdot \sum_{s=fat}^{water} \cdot (S_s(\theta_i) - f_i \times \bar{S}_s)^2) \tag{1}
$$

where $\vec{\theta}$ denotes the flip angle schedule across all TRs, $\lambda_{1,2,3}$ represents the weighting coefficient for each term in the formulation (controlling the relative importance of the three corresponding criteria), the first component of the cost function aims to minimize T_1 bias, the second component of the cost function aims to promote SNR, the last component of the cost function aims to minimize blurring, $\vec{f}$ is a desired k-space weighting profile to modulate the smoothness for both fat and water signals, $S_{fat/water}$ denotes signal of fat or water which is a function of flip angle schedule $\vec{\theta}$ and is determined by Bloch equation simulation with given tissue relaxation parameters ($T_{1, water/fat}$), $\bar{S}_{fat\ or\ water}$ denotes mean signal of fat or water across the whole acquisition. Note that the current implementation imposes no further constraints on the desired flip angles. Specific choices of $\lambda_{1,2,3}$, $\vec{f}$, and assumed $T_{1, water/fat}$ used in this work are described below in the Methods section.

3 | METHODS

3.1 | Flip Angle Design

The proposed flip angle optimization formulation (Equation-1) was evaluated using different combinations of $\lambda_{1,2,3}$ and desired k-space weighting profile, as demonstrated in Figure 1.

For the rest of the study, the values of $\lambda_{1,2,3}$ were empirically set to 1000, 25, and 50, respectively, based on desired features of the water and fat signal profiles (i.e., low discrepancy between fat and water signal, higher overall fat and water signal, and smooth signal profile for both fat and water). Also, the k-space weighting profile $\vec{f}$ was a normalized Gaussian function with variance $\sigma^2 = k_{y,max}$. The predetermined parameters used for flip angle design were $T_{1,water}$ = 809 ms[26] (3T), $T_{1,fat}$ = 382 ms[26] (3T), and TR = 10 ms. Numerical simulations were performed to study the effects of different combinations of $T_{1,water}$ and $T_{1,fat}$ with the proposed method (see Supporting Information Figure S1 under Supplementary Material). With the formulation described in Equation 1 above, a conjugate-gradient algorithm was applied to determine the optimal flip angle schedule. Flip angle optimizations and simulations were implemented in MATLAB (MathWorks, Natick, MA, USA). The flip angles for each TR in the proposed VFA method are reported within the Supplementary Material (Supporting Information Table S1).

3.2 | Numerical Simulation

Numerical simulation experiments were performed in this study to compare the proposed VFA-centric method with current 2D CSE-MRI sequential methods. A digital phantom was designed containing twenty compartments ('vials') with five varying target PDFF values (0%, 10%, 20%, 30%, and 40%) and four varying $J_{1,water}$ (300ms, 600ms, 900ms and 1200 ms) per target PDFF value. Within the simulation experiments, fve different 2D CSE-MRI acquisitions were included for comparison. The fve different CSE-MRI acquisitions were constant low flip angle(3°) with linear phase encoding (denoted as LFA-linear), constant high flip angle(15°) with linear phase encoding (HFA-linear), constant low flip angle(3°) with centric-ordered phase encoding (LFA-centric), constant high flip angle(15°) with centric-ordered phase encoding (HFA-centric), and VFA with centric-ordered phase encoding (VFA-centric). The detailed descriptions of the fve 2D CSE-MRI acquisitions are listed in Table 1. In each case, a six-echo acquisition was simulated with frst TE at 1.2 ms and increment of 1.2 ms for subsequent echoes. All simulations were performed using MATLAB (MathWorks, Natick, MA, USA).

3.3 | Phantom study

A physical phantom containing multiple vials with different PDFF values, as well as different values of $T_{1,water}$, was constructed with same design as the digital phantom used in numerical simulation experiments. The phantom included a total of twenty vials (high-density polyethylene cylindrical vial with volume of 25 mL and diameter of 20 mm). Five different target fat fraction values (nominal PDFF = 0%, 10%, 20%, 30%, and 40%) were obtained by adding appropriate volumes of peanut oil. Four vials with different target values of $T_{1,water}$ (300 ms, 600 ms, 900 ms and 1200 ms) per nominal PDFF value were constructed by using different $CuSO_4$ concentrations (4 mM, 2 mM, 1 mM, 0.5 mM). The phantom construction was based on a previously described agar-based oil-water emulsion approach[27, 28, 29].

The phantom was scanned on a 3T clinical MRI system (Discovery MR750, GE Healthcare, Waukesha, WI) using an 8-channel phased-array head coil. Multi-echo 2D CSE-MRI data were acquired for PDFF mapping. Five different 2D CSE-MRI acquisitions were performed,

with the same flip angle and encoding approaches as in the numerical simulation. For each acquisition, ten repetitions were performed in order to enable pixel-by-pixel assessment of noise performance. Acquisition parameters included slice number = 5, thickness = 5 mm, $N_x \times N_y$=144×144, FOV = 20×20 cm^2, echo train length = 6, single echo train, TE_1 = 1.4 ms, $\triangle TE$ = 2 ms, TR = 12 ms, and BW = ±62.5 Hz. Single-voxel spectroscopy was acquired using a multi-TR-TE stimulated echo acquisition mode (STEAM) MRS sequence[30]. STEAM-MRS was obtained in a cubic voxel which was prescribed as 15×15×15 mm^3 near the center of each vial. $T_{1,\text{water}}$ and $T_{1,fat}$ obtained with spectroscopy data for each vial were used in correction of residual T_1 bias in PDFF measurement from the LFA-linear acquisition, which was used as reference as described below.

3.4 | In vivo Study

In this IRB-approved and HIPAA-compliant study, thirty fve subjects without expected liver disease were recruited with informed written consent. Subjects included 8 adults (5 male/3 female, age: 31.1±7.8, BMI: 23.5±4.2 kg/m^2) and 27 children (20 male/7 female, age: 14.2±2.1, BMI: 20.7±4.3 kg/m^2). All subjects were imaged on the same 3T clinical MRI system used in the phantom study. In vivo imaging was performed with a 32-channel phased-array torso coil. Five different free breathing 2D Cartesian sequential CSE-MRI acquisitions were performed, similarly to the phantom study described above. Acquisition parameters for 2D sequences included slice number = 22, slice thickness = 8 mm, slice gap = 2 mm, $N_x \times N_y$=160×144, FOV = 40× 40 cm^2, echo train length = 6, single echo train, TE_1 = 1.2 ms, $\triangle TE$ = 1.5 ms, TR = 10 ms, BW = ±62.5 Hz, acquisition time = 32 s, acquisition time per slice = 1.4 s, and no parallel imaging. In addition, a standard breath-held 3D CSE-MRI acquisition (denoted as 3D) was performed as well. Acquisition parameters for the 3D sequence included slice number = 28, thickness = 8 mm, $N_x \times N_y$=160× 144, FOV = 40×40 cm^2, flip angle = 3°, echo train length = 3, two echo trains (for a total of 6 echoes), TE_1 = 1.1 ms, $\triangle TE$ = 1 ms, TR = 7.3 ms, BW = ±125 Hz, acquisition time = 19 s, parallel imaging = 2×2, and effective acceleration factor = 3.5. Single-voxel spectroscopy data were obtained using a multi-TR-TE STEAM-MRS sequence[30] and a cubic voxel was prescribed as 20×20×20 mm^3 in the right lobe of the liver. $T_{1,\text{water}}$ and $T_{1,fat}$ obtained from spectroscopy data for each subject were used to correct residual T_1 bias in PDFF measurement from the LFA-linear acquisition, which was used as reference as described below.

3.5 | PDFF Mapping

As demonstrated in previous works, the acquired signal which arises from both fat and water within a voxel can be modeled as follows:

$$S(TE_n) = e^{i \cdot 2\pi \cdot f_B \cdot TE_n} \cdot e^{-R_2^* \cdot TE_n} \cdot (\rho_W + \rho_F \cdot \sum_{p=1}^{6} \alpha_p \cdot e^{i \cdot 2\pi \cdot f_p \cdot TE_n}), \; for \; n = 1, ..., N \tag{2}$$

where S is the signal at each echo time TE_n and N is the total echo number, ρ_F and ρ_W are the amplitudes of the fat and water components, respectively, α_p are the (pre-calibrated) relative amplitudes for the six modeled fat peaks such that $\sum_{p=1}^{6} \alpha_p = 1$, f_p are the relative

frequencies of the six fat components, f_B is the local frequency shift due to static field inhomogeneity[31], and R2* (i.e., 1/T2*) is the transverse relaxation rate.

Following fat-water separation as described above, PDFF was calculated as follows[12, 13, 14, 15]:

$$PDFF = \frac{\rho_F}{\rho_F + \rho_W} \tag{3}$$

where ρ_F and ρ_W are the proton-density weighted signals from fat and water, respectively.

Multi-echo images were fitted using the above signal model (Equation-2) and PDFF formulation(Equation-3) for PDFF estimation. Both the simulation echo images and source CSE-MRI data from the phantom and in vivo studies were processed offline using a magnitude-based PDFF mapping algorithm [27, 31] that corrects for relevant confounding factors (including R2* decay [32], spectral complexity of fat signals [32], temperature effects in phantom experiments [28], residual phase errors [33, 34], and noise bias[20]). PDFF mapping was implemented in MATLAB (MathWorks, Natick, MA).

Spectroscopy data from the STEAM-TE-TR acquisitions[30] were processed offline using an automated custom algorithm[35] that jointly fits all the acquired spectra and simultaneously estimates $T_{1,water}$ and $T_{1,fat}$, among other parameters. The processing script was implemented in MATLAB (MathWorks, Natick, MA).

3.6 | Measurements and Statistical Analysis

For numerical simulation experiments, flip angle schedule and relative signal intensity of fat and water were compared across different acquisitions. Reconstructed PDFF maps from each acquisition, as well as the PDFF difference maps between each reconstructed PDFF map and the ground truth PDFF map were displayed to illustrate T_1 bias effects, SNR performance, and blurring artifacts.

For the phantom experiments, a region of interest (ROI) with circular shape (with area of approximately 1.5 cm^2) was placed in the center of each vial within the central slice, in order to measure mean PDFF value from PDFF map for each vial and each repetition. Further, pixel-wise maps of PDFF standard deviation were obtained from the ten repeated acquisitions. The same ROIs were used to measure the mean PDFF standard deviation (as a surrogate measurement of SNR) for each acquisition. PDFF bias was calculated as the difference between mean measured PDFF and reference PDFF. The reference PDFF value for each vial was obtained from the LFA-linear-based PDFF, corrected for any residual T1 bias by using the vial-specific $T_{1,water}$ and $T_{1,fat}$ (measured from STEAM-MRS). Linear mixed-effects model analysis was performed for comparison across the fve 2D CSE-MRI acquisitions, using the following model for observed PDFF bias: PDFF$_{bias}$ ~1+true PDFF +$T_{1,water}$+true PDFF· $T_{1,water}$. The true PDFF used in this model was the reference PDFF described above and the $T_{1,water}$ in this model was the vial-specifc $T_{1,water}$ obtained from spectroscopy data.

For the in vivo data, a circular ROI (with area of approximately 16 cm^2) was drawn in the right lobe of liver (in Couinaud segment VI or VII) for each acquisition, while avoiding large blood vessels and bile ducts. All ROIs were carefully chosen to avoid motion artifacts. Mean and standard deviation of PDFF were recorded for each ROI. Mean PDFF measurements were analyzed using linear correlation and Bland-Altman analysis between the PDFF measured from different MR acquisitions (i.e., 2D acquisitions and 3D acquisition) and the reference PDFF (obtained from the LFA-linear acquisition, corrected for any residual T$_1$ bias). The measured standard deviation of PDFF across the ROI (as a surrogate measure of SNR) was plotted for each of the acquisitions (i.e., fve 2D acquisitions and one 3D acquisition), and the minimum, maximum, and median standard deviation across subjects were displayed for each acquisition as well. Bonferroni corrected t-tests were performed between fve CSE-MRI acquisitions (3D, LFA-linear, HFA-linear, LFA-centric, and HFA-centric) and the proposed VFA-centric acquisition. All statistical analyses were performed with MATLAB (MathWorks, Natick, MA) and Python.

4 | RESULTS

4.1 | Numerical Simulation

Figure 1 represents fat and water signal profiles across the phase encoding direction in k-space, with different choices of parameters for the proposed flip angle optimization formulation (Equation-1). Specifcally, different values of the regularization parameters λ_1 and λ_2, as well as the shape of the desired k-space weighting profile were evaluated. For each of these three parameters, Figure 1 depicts the fat and water signal profiles for three different choices of the parameter value. Figure 1(a-c) depicts the effect of λ_1, which penalizes T$_1$ bias in the acquisition. With increasing λ_1, the signals from fat and water become very similar, at the cost of reduced overall signal. Figure 1(d-f) depicts the effect of λ_2, which promotes high signal (i.e., high SNR). With increasing λ_2, fat and water signals are both increased, at the cost of slight differences between fat and water signal profiles. Finally, fgure 1(g-i) depicts the effect of the desired k-space weighting profle. Indeed, choosing a flat profle (Figure 1(g)) leads to slightly reduced signal at the center of k-space compared to Gaussian-shaped profiles (Figure 1(h-i)), which in turn lead to increased k-space fltering.

Simulation-based comparisons among fve different 2D CSE-MRI acquisitions (LFA-linear, HFA-linear, LFA-centric, HFA-centric, and VFA-centric) are illustrated in Figure 2, including the corresponding flip angle design, relative signal intensity profle of fat and water across the phase encoding direction, and PDFF map. For acquisitions using constant low flip angles (LFA-linear and LFA-centric), either with linear phase encoding or centric-ordered phase encoding, the signal intensity of fat and water is flat and relatively low across k-space. The flat signal profile results in negligible blurring artifacts and limited T$_1$ bias in PDFF estimation. However, these acquisitions lead to low SNR (high noise level), as shown in the PDFF map and the PDFF difference map. For acquisitions using constant high flip angle (HFA-linear and HFA-centric), SNR performance is improved with higher signal intensity. However, the signal intensity profiles are different between linear and centric-ordered phase encoding strategies. The signal intensity of fat and water within the first TR are the same for

either linear phase encoding or centric-ordered phase encoding. HFA-linear acquisition causes divergence of fat and water signals across the phase encoding steps (i.e., from negative k_y to positive k_y), leading to large T_1 bias in PDFF estimation, as illustrated in the PDFF map and the PDFF difference map. HFA-centric acquisition causes a fat and water signal divergence that is approximately symmetric with respect to $k_y = 0$, with both fat and water signal profiles decaying rapidly away from the center of k-space. This filtered signal profile results in blurring artifacts which can be observed in the PDFF map and the PDFF difference map. The proposed VFA-centric acquisition has higher signal intensity than low flip angle acquisitions (by a factor of approximately 2.2 in the center of k-space), with less filtering than the HFA-centric acquisition and little divergence between fat and water signal (i.e., minimal T_1 bias). The PDFF map obtained with the VFA-centric acquisition provides simultaneously low T_1 bias, high SNR (compared to alternative 2D acquisitions), and low blurring in fat quantification.

4.2 | Phantom study

$T_{1,water}$ values in each vial of the phantom are summarized in Table 2. $T_{1,fat}$ for all vials with PDFF>0% is within 350 ±12 ms. PDFF bias (i.e., difference between measured PDFF and reference PDFF which was obtained from LFA-linear acquisition with correction for residual T_1 bias) analysis across various PDFF levels is demonstrated in Figure 3 for five different MR acquisitions (LFA-linear, HFA-linear, LFA-centric, HFA-centric, and VFA-centric). For the four vials with PDFF = 0%, PDFF bias is small for all five acquisitions. HFA-linear acquisition results in the highest PDFF bias among all acquisitions across different PDFF levels. Also, PDFF bias increases with increasing $T_{1,water}$, as expected when using a constant high flip angle schedule during acquisition. However, LFA-linear, LFA-centric, HFA-centric, and the proposed VFA-centric acquisitions enabled low PDFF bias in the range of −3% to 3%. In summary, the proposed VFA-centric method leads to PDFF estimation with low bias across a wide range of $T_{1,water}$ and PDFF values.

In the box plots of Figure 3, the vertical range of each acquisition represents the pixel-wise standard deviation of the ROI measurements from ten repetitions. Within various PDFF levels and $T_{1,water}$, LFA-linear and LFA-centric acquisitions have higher standard deviation (i.e., lower SNR) for PDFF measurements than the other three acquisitions (HFA-linear, HFA-centric, and VFA-centric). Using the standard deviation of the PDFF measurement as a surrogate measure of SNR, the proposed VFA-centric acquisition is able to obtain approximately twice the SNR of the reference acquisition (LFA-linear). All standard deviation values of each vial of the phantom are reported within the Supplementary Material (Supporting Information Table S2).

Linear mixed-effects model results regarding PDFF bias for the five different CSE-MRI acquisitions (LFA-linear, HFA-linear, LFA-centric, HFA-centric, and VFA-centric) are detailed inTable 3. For the reference LFA-linear acquisition and LFA-centric acquisition, none of the factors considered (true PDFF, $T_{1,water}$, and product of true PDFF with $T_{1,water}$) contribute significantly to PDFF bias (p > 0.01). For HFA-linear acquisition, true PDFF, $T_{1,water}$, and product of true PDFF with T_{water} each has a highly significant effect on PDFF bias (p < 0.01). For HFA-centric acquisition, true PDFF has a highly significant effect on

PDFF bias ($p < 0.01$) and product of true PDFF with $T_{1,water}$ has a mildly significant effect on PDFF bias ($p = 0.04$). For the proposed VFA-centric acquisition, true PDFF has a weak significant effect on PDFF bias ($p = 0.05$). However, this effect is small: -0.06 ± 0.03. Finally, in VFA-centric acquisition, neither of the $T_{1,water}$ or the product of true PDFF with $T_{1,water}$ contributes significantly to PDFF bias ($p > 0.05$).

4.3 | In vivo Study

In the in vivo study, a mean TOFF value of 4.6% over a range of 1.4-38.1%, with a standard deviation of 7.1% was observed across all subjects. Representative PDFF maps from two children under three different CSE-MRI acquisitions (3D, LFA-linear, and VFA-centric) are shown in Figure 4. PDFF maps obtained with these three acquisitions show negligible motion artifact and high image quality for the child who was able to maintain a breath-hold during the 3D acquisition. In contrast, a child who was unable to hold breath during scanning results in substantial motion artifacts in the 3D acquisition. Free breathing 2D methods, either the LFA-linear acquisition or the proposed VFA-centric acquisition, effectively freeze respiratory motion during acquisition and provide artifact-free PDFF maps. In both subjects, the free breathing 2D method using the proposed VFA-centric approach showed visually apparent improvement in SNR performance compared to the reference LFA-linear acquisition.

PDFF maps from three adults with different PDFF levels are demonstrated with three different CSE-MRI acquisitions (3D, LFA-linear, and VFA-centric) in Figure 5. All three adult subjects were able to perform adequate breath-holds during the 3D acquisition. These subjects had low PDFF (~2%), moderately high PDFF (~11%), and very high PDFF (~39%) in the liver, respectively. These three acquisitions (3D, LFA-linear, VFA-centric) have good agreement in liver fat quantification for these three subjects. LFA-linear acquisition results in low SNR which might complicate the assessment of lobar distribution of fat in the second and the third subject. In contrast, the proposed VFA-centric acquisition provides motion robustness (compared with 3D acquisition) with high SNR (compared with previous 2D sequential acquisitions), and PDFF measurements in good agreement with the 3D BH method across different fat fraction levels.

Linear regression analysis results comparing measured PDFF from each acquisition (3D, HFA-linear, LFA-centric, HFA-centric, and VFA-centric) and reference PDFF across all subjects are shown on the top row of Figure 6. In these results, 3D, LFA-centric, and HFA-centric acquisitions show high correlation with the reference acquisition (LFA-linear). The slopes of the correlation are between 1.00 to 1.02 with R^2 between 0.987 to 0.996. However, the correlation relationship between HFA-linear acquisition and reference acquisition (LFA-linear) has a slope of $1.14\pm0.48\times10^{-3}$, an intercept of 0.36 ± 0.03, and R^2 equals 0.989. The proposed VFA-centric acquisition shows high agreement with the reference acquisition (LFA-linear) and the correlation relationship has a slope of $1.00\pm0.05\times10^{-3}$, an intercept of $0.04\pm3.47\times10^{-3}$, and R^2 equals 0.998. Results of Bland-Altman analysis are shown on the bottom row of Figure 6. 3D and LFA-centric acquisitions show small PDFF bias. The 95% LoA is between -1.0% to 1.0%. HFA-linear and HFA-centric acquisitions show relatively large PDFF bias. The 95% LoA is between -1.6% to 3.6%. The proposed VFA-centric

acquisition has a very small bias (0.0%) and narrow 95% LoA (−0.5% to 0.6%) compared with the reference acquisition (LFA-linear) in fat quantification.

Figure 7 depicts the comparisons between six different CSE-MRI acquisitions (3D, LFA-linear, HFA-linear, LFA-centric, HFA-centric, and VFA-centric) regarding intra-ROI PDFF standard deviation distribution across all subjects. Intra-ROI PDFF standard deviation is used as a surrogate measure of SNR of each acquisition. LFA-linear and LFA-centric acquisitions have relatively low SNR performance with high mean standard deviation (LFA-linear = 3.3%, LFA-centric = 3.3%). HFA-linear and HFA-centric acquisitions have relatively high SNR performance with low mean standard deviation (HFA-linear = 1.4 %, HFA-centric = 1.1%). The proposed VFA-centric acquisition has relatively high SNR performance with low mean standard deviation of 1.5%. Bonferroni-corrected t-test results are demonstrated in Figure 7 as well. The proposed VFA-centric acquisition shows significantly lower standard deviation than LFA-linear acquisition ($p < 0.001$) and LFA-centric acquisition ($p < 0.001$), although with higher standard deviation than HFA-centric acquisition ($p = 0.006$), and no significant difference than LFA-centric acquisition ($p = 0.20$).

5 | DISCUSSION

In this work we have proposed a novel motion-robust free-breathing 2D sequential CSE-MRI method that uses an optimized variable flip angle schedule and centric-ordered phase encoding to quantify PDFF while minimizing T_1-related bias and image blurring. Low bias in PDFF estimation was verified using a custom designed phantom with varying $T_{1,water}$ and varying PDFF. In vivo, the proposed VFA-centric method has high image quality (low blurring), low bias, and high SNR compared to a recently proposed 2D sequential low flip angle acquisition.

This proposed free breathing 2D Cartesian CSE-MRI VFA-centric method overcomes existing drawbacks of conventional 3D Cartesian and 2D Cartesian methods. In practice, young children, the elderly and sick patients are often unable to sustain a prolonged breath-hold. By enabling reliable PDFF mapping without the need for breath-holding or respiratory triggering, the proposed VFA-centric method may enable improved imaging workflow in the clinic as well as in research studies, particularly those involving children. In addition, this method may have implications for other emerging applications where there is substantial non-periodic motion, including fetal imaging applications [36]. Finally, the proposed VFA-centric method may enable 2D CSE-MRI to perform reliably in low SNR situations where the LFA-linear approach may fail, such as in the presence of liver iron overload. The effective SNR gain is about 2.2 from the proposed VFA-centric method compared to LFA-linear method, as predicted through signal simulations as well as measured from liver scans in this work.

There are various other existing CSE-MRI methods aiming to reduce motion artifacts and achieve high SNR for liver fat quantification. Respiratory-gated Cartesian 3D CSE-MRI methods [17], non-Cartesian methods including a 3D stack-of-radial approach [18] and a 3D spiral approach [37], and compressed sensing methods[38, 39] all have demonstrated

promising performance in previous works. In the context of these existing methods, the proposed VFA-centric method has two desirable features: inherent motion robustness due to the short temporal footprint, and simple reconstruction and processing due to the 2D Cartesian acquisition. Importantly, combination of the proposed VFA-centric method with respiratory gated, non-Cartesian, or compressed sensing methods may offer opportunities to combine the strengths of these methods in future work.

This study had several limitations. The proposed VFA-centric acquisition is performed with single echo train and no parallel imaging for simplicity of the optimization formulation. It is feasible to extend the proposed VFA-centric method with parallel imaging and multi-echo-train acquisition in the future. An inherent limitation of free breathing 2D acquisitions is the slice misalignment between different slices. However, this may be acceptable in the context of diffuse liver disease. Importantly, for all measurements in this study, ROIs in 2D and 3D slices were carefully co-localized based on similarity of anatomic structures. Further, emerging methods[21] may be able to address misalignment in free-breathing multi-repetition acquisitions. R2* quantification using the proposed VFA-centric acquisition is also feasible but was not included in this study due to the lack of subjects with liver iron overload (i.e., high R2*). A study including subjects with a wide range of liver R2* is considered as future work for R2* mapping using the proposed method.

One technical limitation of the proposed flip angle optimization is that the global minimum is not guaranteed to be achieved due to the non-convex nature of the optimization problem. Further, in this work, different combinations of the formulation parameters including three weighting terms ($\lambda 1$, λ_2, and λ_3) and one desired k-space weighting profile ($\overrightarrow{f}$) were evaluated in order to enable simultaneous low T_1 bias, high SNR, and minimal blurring. Our early results indicate that the proposed approach is able to provide a desirable balance between these three competing goals. However, further optimization of the formulation parameters is likely possible. Another limitation of the proposed method is that the current flip angle schedule optimization problem is solved offline. Development of rapid algorithms to achieve a global minimum is highly desirable as future work. The current validation study also has several limitations, including a limited number of adults and children. Further validation in larger studies is warranted. Also, the distribution of PDFF values observed in the in vivo study (mean PDFF: 4.6%, standard deviation: 7.1%, and range: 1.4-38.1%) was skewed towards low PDFF values, although this distribution was relatively similar to that found in a recent meta-analysis study (mean: 9.6%, standard deviation: 8.8%)[40]. Nevertheless, larger studies including more subjects with NAFLD will be needed in the future to provide further validation of the proposed method.

In conclusion, the proposed 2D Cartesian sequential CSE-MRI method based on a variable flip angle approach with centric-ordered phase encoding enabled motion-robust mapping of PDFF, with a desirable balance among low T_1 bias, high SNR compared to previous 2D sequential methods, and minimal blurring artifact. This approach may enable improved fat quantification in pediatric imaging and other challenging scenarios.

Author Manuscript

Supplementary Material

Refer to Web version on PubMed Central for supplementary material.

Acknowledgements

references

[1]. Sanyal AJ, Banas C, Sargeant C, Luketic VA, Sterling RK, Stravitz RT, et al. Similarities and differences in outcomes of cirrhosis due to nonalcoholic steatohepatitis and hepatitis C. Hepatology 2006;43(4):682–689. [PubMed: 16502396]

[2]. Rubinstein E, Lavine JE, Schwimmer JB. Hepatic, cardiovascular, and endocrine outcomes of the histological subphenotypes of nonalcoholic fatty liver disease In: Seminars in liver disease, vol. 28 © Thieme Medical Publishers; 2008 p. 380–385. [PubMed: 18956294]

[3]. Ekstedt M, Franzén LE, Mathiesen UL, Thorelius L, Holmqvist M, Bodemar G, et al. Long-term follow-up of patients with NAFLD and elevated liver enzymes. Hepatology 2006;44(4):865–873. [PubMed: 17006923]

[4]. Hazlehurst JM, Woods C, Marjot T, Cobbold JF, Tomlinson JW. Non-alcoholic fatty liver disease and diabetes. Metabolism 2016;65(8):1096–1108. [PubMed: 26856933]

[5]. Puchner SB, Lu MT, Mayrhofer T, Liu T, Pursnani A, Ghoshhajra BB, et al. High-risk coronary plaque at coronary CT angiography is associated with nonalcoholic fatty liver disease, independent of coronary plaque and stenosis burden: results from the ROMICAT II trial. Radiology 2014;274(3):693–701. [PubMed: 25369449]

[6]. Fargion S, Porzio M, Fracanzani AL. Nonalcoholic fatty liver disease and vascular disease: state-of-the-art. World journal of gastroenterology: WJG 2014;20(37):13306. [PubMed: 25309067]

[7]. Mantovani A, Pernigo M, Bergamini C, Bonapace S, Lipari P, Pichiri I, et al. Nonalcoholic fatty liver disease is independently associated with early left ventricular diastolic dysfunction in patients with type 2 diabetes. PLoS One 2015;10(8):e0135329. [PubMed: 26252899]

[8]. Mantovani A, Rigamonti A, Bonapace S, Bolzan B, Pernigo M, Morani G, et al. Nonalcoholic fatty liver disease is associated with ventricular arrhythmias in patients with type 2 diabetes referred for clinically indicated 24-hour Holter monitoring. Diabetes Care 2016;39(8):1416–1423. [PubMed: 27222503]

[9]. Feldstein AE, Charatcharoenwitthaya P, Treeprasertsuk S, Benson JT, Enders FB, Angulo P. The natural history of nonalcoholic fatty liver disease in children: a follow-up study for up to 20 years. Gut 2009;58(11):1538–1544. [PubMed: 19625277]

[10]. Pan L, Blanck HM, Sherry B, Dalenius K, Grummer-Strawn LM. Trends in the prevalence of extreme obesity among US preschool-aged children living in low-income families, 1998-2010. Jama 2012;308(24):2563–2565. [PubMed: 23268509]

[11]. Ordonez R, Carbajo-Pescador S, Mauriz J, Gonzalez-Gallego J. Understanding nutritional interventions and physical exercise in non-alcoholic fatty liver disease. Current molecular medicine 2015;15(1):3–26. [PubMed: 25601465]

[12]. Meisamy S, Hines CD, Hamilton G, Sirlin CB, McKenzie CA, Yu H, et al. Quantification of hepatic steatosis with T1-independent, T2*-corrected MR imaging with spectral modeling of fat:

blinded comparison with MR spectroscopy. Radiology 2011;258(3):767–775. [PubMed: 21248233]

[13]. Hines CD, Frydrychowicz A, Hamilton G, Tudorascu DL, Vigen KK, Yu H, et al. T1 independent, T2* corrected chemical shift based fat–water separation with multi-peak fat spectral modeling is an accurate and precise measure of hepatic steatosis. Journal of magnetic resonance imaging 2011;33(4):873–881. [PubMed: 21448952]

[14]. Yokoo T, Bydder M, Hamilton G, Middleton MS, Gamst AC, Wolfson T, et al. Nonalcoholic fatty liver disease: diagnostic and fat-grading accuracy of low-flip-angle multiecho gradient-recalled-echo MR imaging at 1.5 T. Radiology 2009;251(1):67–76. [PubMed: 19221054]

[15]. Yokoo T, Shiehmorteza M, Hamilton G, Wolfson T, Schroeder ME, Middleton MS, et al. Estimation of hepatic proton-density fat fraction by using MR imaging at 3.0 T. Radiology 2011;258(3):749–759. [PubMed: 21212366]

[16]. Pooler BD, Hernando D, Ruby JA, Ishii H, Shimakawa A, Reeder SB. Validation of a motion-robust 2D sequential technique for quantification of hepatic proton density fat fraction during free breathing. Journal of Magnetic Resonance Imaging 2018;48(6):1578–1585. [PubMed: 29665193]

[17]. Motosugi U, Hernando D, Bannas P, Holmes JH, Wang K, Shimakawa A, et al. Quantification of liver fat with respiratory-gated quantitative chemical shift encoded MRI. Journal of Magnetic Resonance Imaging 2015;42(5):1241–1248. [PubMed: 25828696]

[18]. Armstrong T, Dregely I, Stemmer A, Han F, Natsuaki Y, Sung K, et al. Free-breathing liver fat quantification using a multiecho 3 D stack-of-radial technique. Magnetic resonance in medicine 2018;79(1):370–382. [PubMed: 28419582]

[19]. Ruby J, Hernando D, Campo C, Shimakawa A, Reeder S, Johnson K. Motion insensitive quantification of liver proton density fat-fraction using a single-shot 2D technique. In: Proceedings of the AnnualMeeting of the International Society for Magnetic Resonance in Medicine, Singapore, Singapore; 2016.

[20]. Liu C, McKenzie C, Yu H, Brittain J, Reeder S. Fat quantification with IDEAL gradient echo imaging: correction of bias from T1 and noise. Magnetic Resonance in Medicine 2007;58(2):354–364. [PubMed: 17654578]

[21]. Luo H, Wiens C, Campo C, Shimakawa A, Reeder SB, Johnson K. A novel fat and iron quantification technique with nonrigid motion-corrected averaging based on non-local means. In: Proceedings of the Annual Meeting of the International Society for Magnetic Resonance in Medicine, Honolulu, US; 2017.

[22]. Deppe MH, Wild JM. Variable flip angle schedules in bSSFP imaging of hyperpolarized noble gases. Magnetic resonance in medicine 2012;67(6):1656–1664. [PubMed: 22134846]

[23]. Fischer SE, McKinnon GC, Scheidegger MB, Prins W, Meier D, Boesiger P. True myocardial motion tracking. Magnetic resonance in medicine 1994;31(4):401–413. [PubMed: 8208116]

[24]. Stuber M, Spiegel M, Fischer S, Scheidegger M, Danias P, Pedersen E, et al. Single breath-hold slice-following CSPAMM myocardial tagging. Magnetic Resonance Materials in Physics, Biology and Medicine 1999;9(1-2):85–91.

[25]. Hennig J, Weigel M, Scheffler K. Calculation of flip angles for echo trains with predefined amplitudes with the extended phase graph (EPG)-algorithm: principles and applications to hyperecho and TRAPS sequences. Magnetic Resonance in Medicine: An Official Journal of the International Society for Magnetic Resonance in Medicine 2004;51(1):68–80.

[26]. De Bazelaire CM, Duhamel GD, Rofsky NM, Alsop DC. MR imaging relaxation times of abdominal and pelvic tissues measured in vivo at 3.0 T: preliminary results. Radiology 2004;230(3):652–659. [PubMed: 14990831]

[27]. Hernando D, Sharma SD, Aliyari Ghasabeh M, Alvis BD, Arora SS, Hamilton G, et al. Multisite, multivendor validation of the accuracy and reproducibility of proton-density fat-fraction quantification at 1.5 T and 3T using a fat–water phantom. Magnetic resonance in medicine 2017;77(4):1516–1524. [PubMed: 27080068]

[28]. Hernando D, Sharma SD, Kramer H, Reeder SB. On the confounding effect of temperature on chemical shift-encoded fat quantification. Magnetic resonance in medicine 2014;72(2):464–470. [PubMed: 24123362]

[29]. Hines CD, Yu H, Shimakawa A, McKenzie CA, Brittain JH, Reeder SB. T1 independent, T2* corrected MRI with accurate spectral modeling for quantification of fat: validation in a fat-water-SPIO phantom. Journal of Magnetic Resonance Imaging: An Official Journal of the International Society for Magnetic Resonance in Medicine 2009;30(5):1215–1222.

[30]. Hamilton G, Middleton MS, Hooker JC, Haufe WM, Forbang NI, Allison MA, et al. In vivo breath-hold 1H MRS simultaneous estimation of liver proton density fat fraction, and T1 and T2 of water and fat, with a multi-TR, multi-TE sequence. Journal of Magnetic Resonance Imaging 2015;42(6):1538–1543. [PubMed: 26114603]

[31]. Hernando D, Kellman P, Haldar J, Liang ZP. Robust water/fat separation in the presence of large field inhomogeneities using a graph cut algorithm. Magnetic Resonance in Medicine: An Official Journal of the International Society for Magnetic Resonance in Medicine 2010;63(1):79–90.

[32]. Yu H, Shimakawa A, McKenzie CA, Brodsky E, Brittain JH, Reeder SB. Multiecho water-fat separation and simultaneous R estimation with multifrequency fat spectrum modeling. Magnetic Resonance in Medicine: An Official Journal of the International Society for Magnetic Resonance in Medicine 2008;60(5):1122–1134.

[33]. Yu H, Shimakawa A, Hines CD, McKenzie CA, Hamilton G, Sirlin CB, et al. Combination of complex-based and magnitude-based multiecho water-fat separation for accurate quantification of fat-fraction. Magnetic resonance in medicine 2011;66(1):199–206. [PubMed: 21695724]

[34]. Hernando D, Hines C, Yu H, Reeder S. Addressing phase errors in fat-water imaging using a mixed magnitude/complex fitting method. Magnetic resonance in medicine 2012;67(3):638–644. [PubMed: 21713978]

[35]. Hernando D, Artz N, Hamilton G, Roldan A, Reeder S. Fully Automated Processing of Multi-Echo Spectroscopy Data for Liver Fat Quantification,. In: Proceedings of the Annual Meeting of the International Society for Magnetic Resonance in Medicine, Milan, Italy; 2014.

[36]. Sinclair KJ, Friesen-Waldner LJ, McCurdy CM, Wiens CN, Wade TP, de Vrijer B, et al. Quantification of fetal organ volume and fat deposition following in utero exposure to maternal Western Diet using MRI. PloS one 2018;13(2):e0192900. [PubMed: 29447203]

[37]. Börnert P, Koken P, Eggers H. Spiral water–fat imaging with integrated off-resonance correction on a clinical scanner. Journal of Magnetic Resonance Imaging 2010;32(5):1262–1267. [PubMed: 21031534]

[38]. Doneva M, Børnert P, Eggers H, Mertins A, Pauly J, Lustig M. Compressed sensing for chemical shift-based water–fat separation. Magnetic resonance in medicine 2010;64(6):1749–1759. [PubMed: 20859998]

[39]. Sharma SD, Hu HH, Nayak KS. Accelerated water–fat imaging using restricted subspace field map estimation and compressed sensing. Magnetic resonance in medicine 2012;67(3):650–659. [PubMed: 21713983]

[40]. Yokoo T, Serai SD, Pirasteh A, Bashir MR, Hamilton G, Hernando D, et al. Linearity, bias, and precision of hepatic proton density fat fraction measurements by using MR imaging: a meta-analysis. Radiology 2017;286(2):486–498. [PubMed: 28892458]
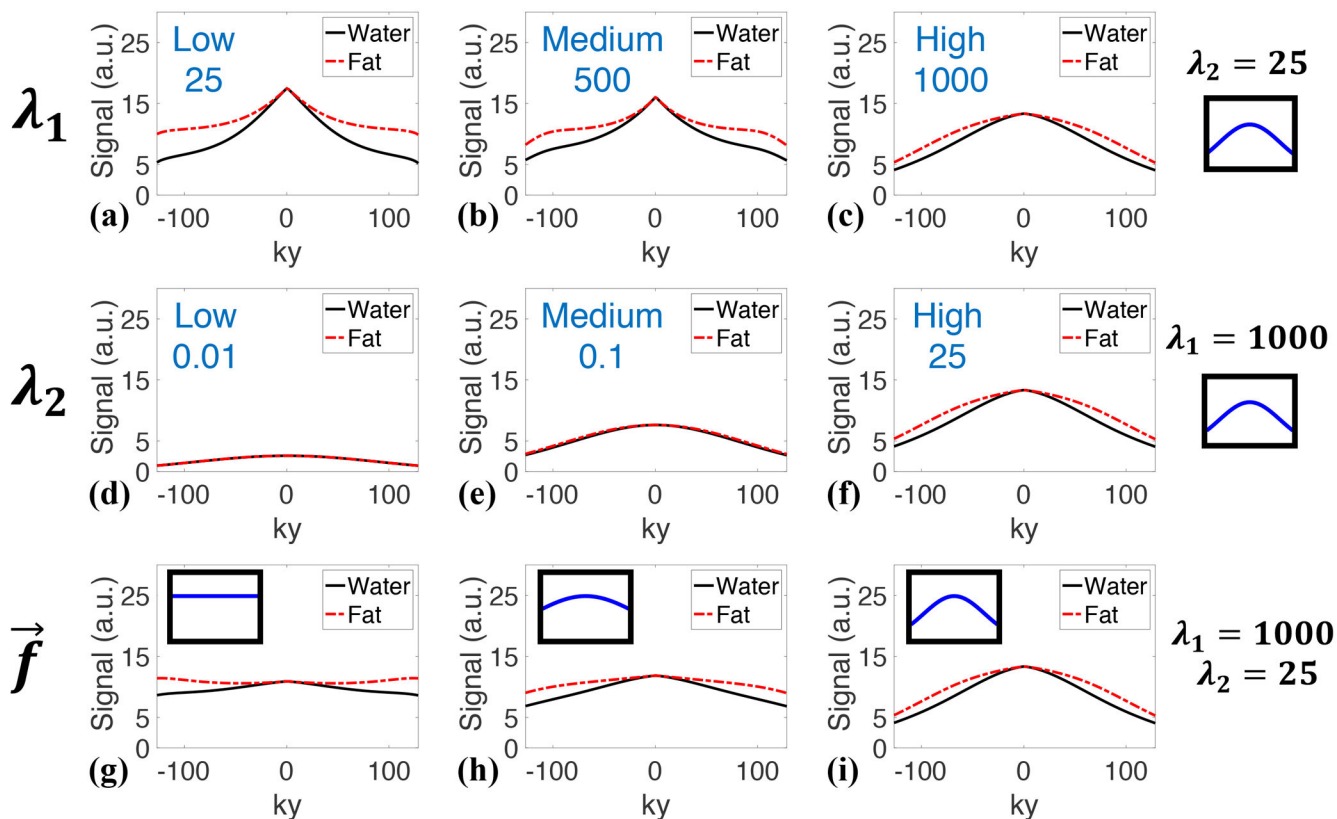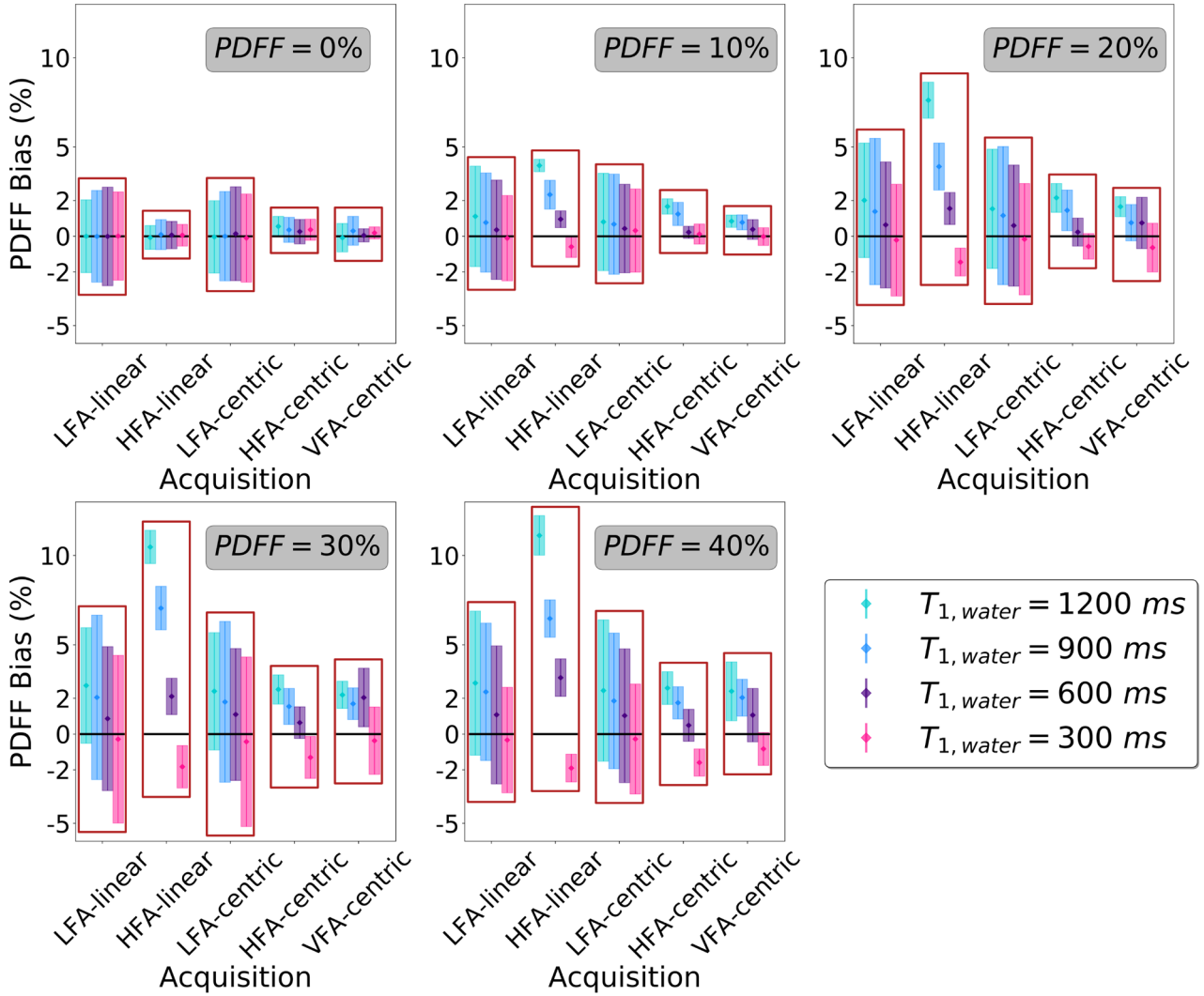
Figure 1.
The proposed formulation enables the generation of various fat and water signal profiles with different trade-offs between T_1 bias, signal level (i.e., SNR), and k-space fltering, based on the choice of several key formulation parameters (i.e., λ_1, λ_2, and k-space weighting profile). (a-c) Increasing values of λ_1, which controls the T_1 bias penalty, lead to reduced T_1 bias (i.e., similar signal profiles for fat and water) at the cost of reduced signal levels. (d-f) Increasing values of λ_2, which controls the signal level, promotes high signal level (i.e., SNR) at the cost of slight differences between fat and water profiles. (g-i) Effects of the desired k-space weighting profile. A flat profile (g) leads to slightly reduced signal at the center of k-space compared to Gaussian-shaped profiles (h-i), which in turn lead to some k-space fltering. The parameter choice in the third column was applied in subsequent experiments in this study.
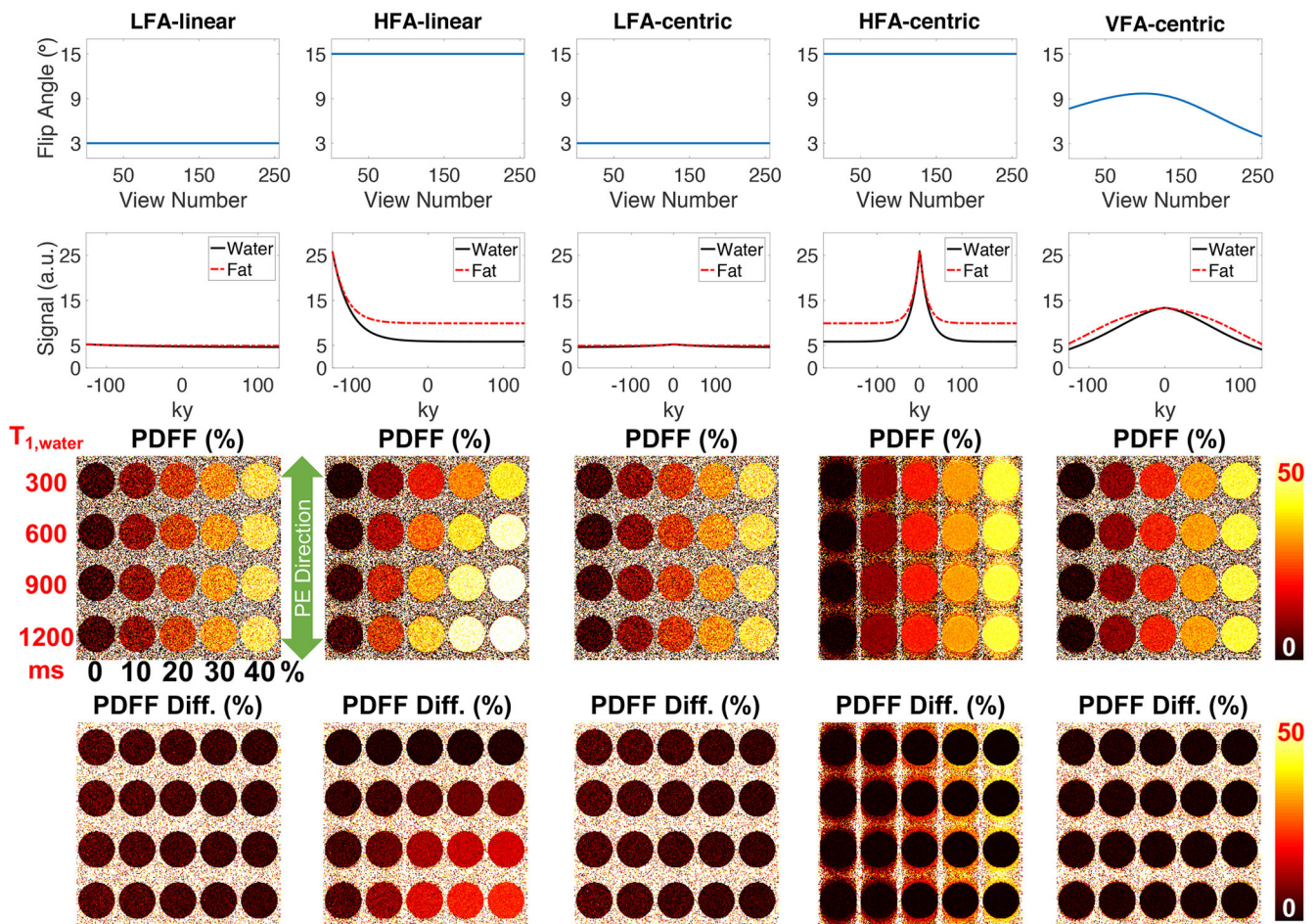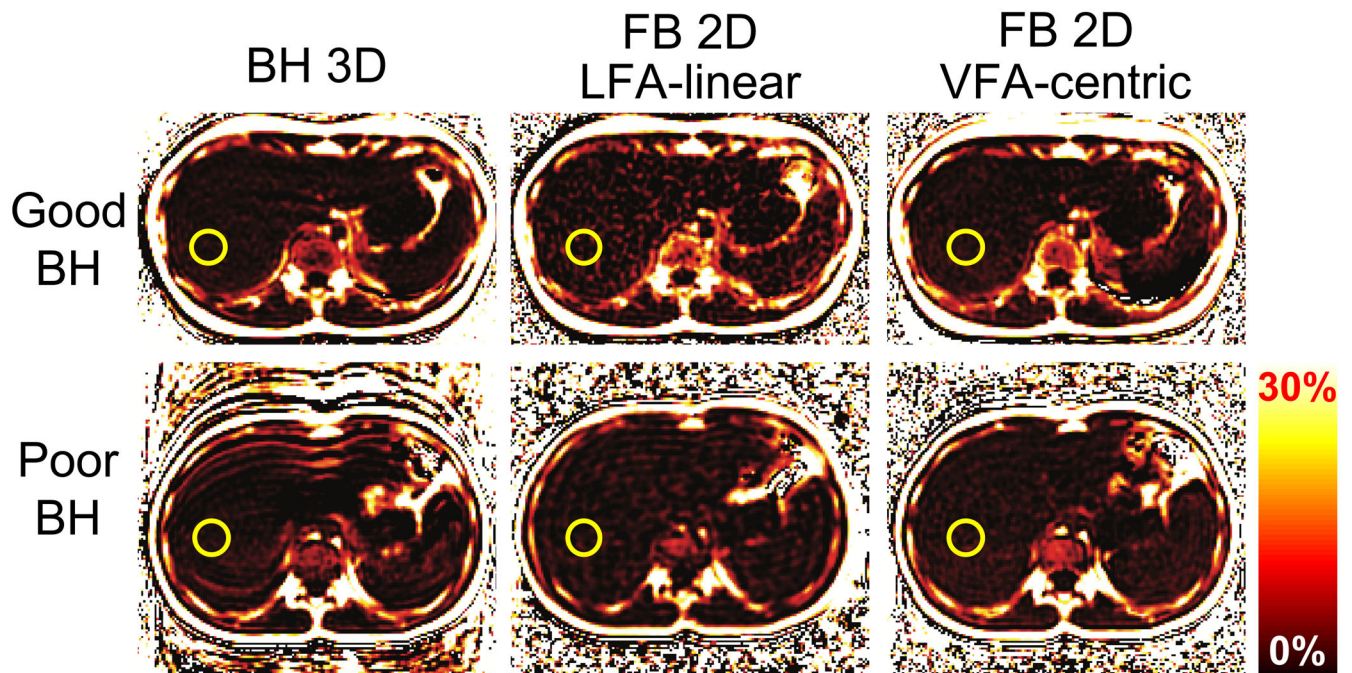
Figure 2.
Simulation-based comparisons between five different 2D CSE-MRI acquisitions (LFA-linear, HFA-linear, LFA-centric, HFA-centric, and VFA-centric), including the corresponding flip angle design (frst row), relative signal intensity profle of fat and water across the phase encoding direction (second row), PDFF map (third row), and PDFF difference map (fourth row). As demonstrated by these simulations, the proposed VFA-centric method provides relatively high signal intensity (high SNR) with little divergence between fat and water (low T_1 bias), and moderate k-space fltering (low blurring).
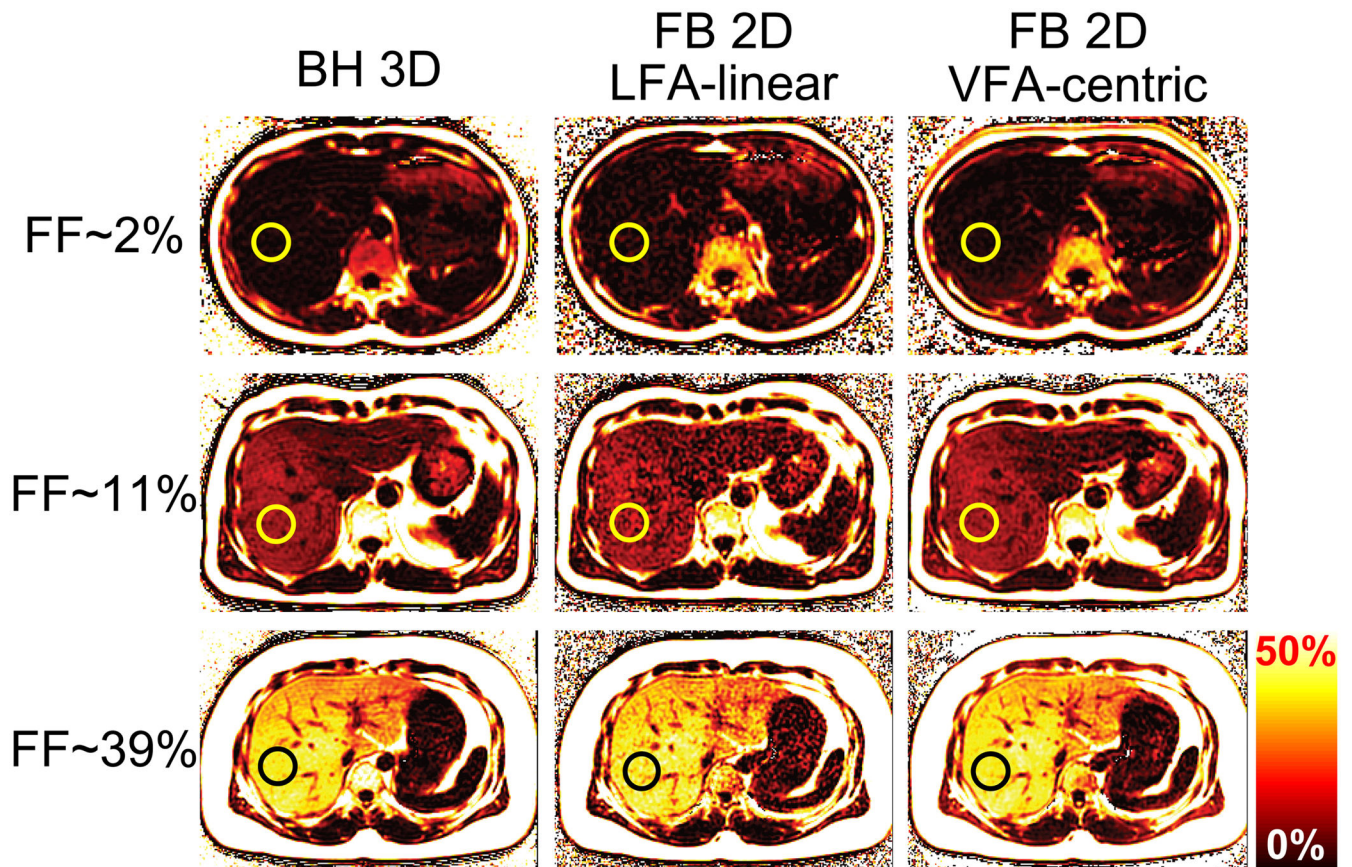
Figure 3.
Results from a PDFF/ T_1 phantom experiment, showing PDFF bias analysis among five different 2D CSE-MRI acquisitions (LFA-linear, HFA-linear, LFA-centric, HFA-centric, and VFA-centric). The vertical range of each acquisition represents the ROI-based pixel-wise standard deviation of the ten repeated experiment measurements. Using standard deviation of PDFF measurement as a surrogate measure of SNR, LFA-linear and LFA-centric acquisitions have higher standard deviation (i.e., lower SNR) for PDFF measurements than HFA-linear, HFA-centric, and the proposed VFA-centric acquisitions. However, HFA-linear acquisition leads to T_1 bias in PDFF measurements. Further, HFA-centric acquisition leads to severe blurring (not shown). The VFA-centric acquisition provides low bias across a wide range of $T_{1,water}$ and PDFF values, and about twice the SNR of the reference acquisition (i.e., LFA-linear).
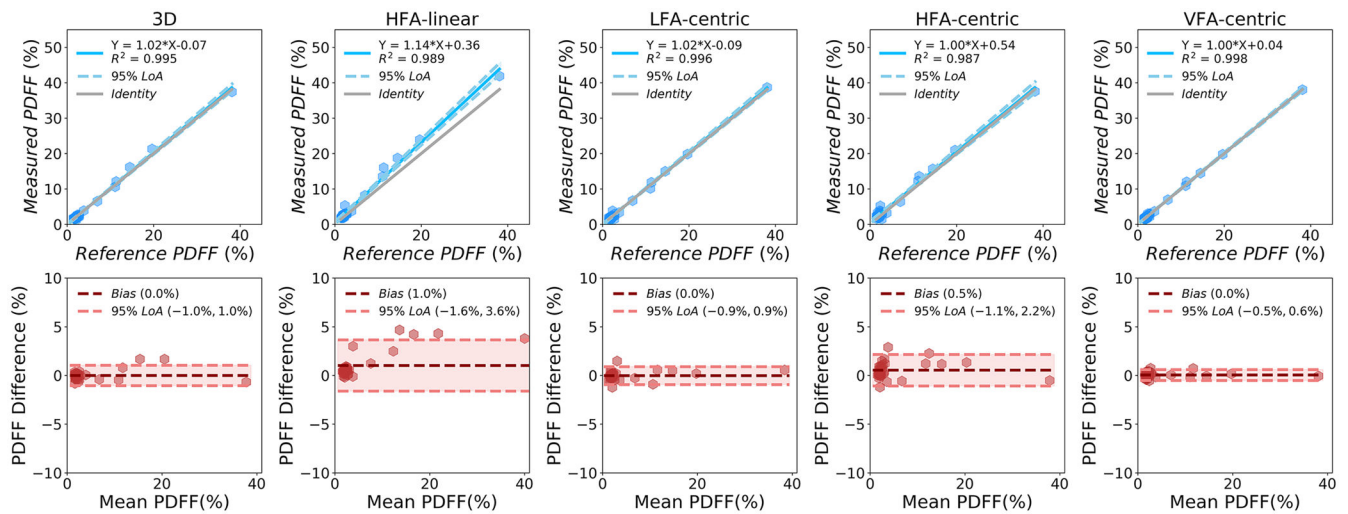
Figure 4.

Representative PDFF maps from two children, obtained with three different CSE-MRI acquisitions (3D, LFA-linear, and VFA-centric). One child was able to sustain a 20-second breath-hold ('Good BH', top row), whereas another child was unable to sustain such breath-hold ('Poor BH', bottom row). In the Good BH case, negligible motion artifacts are observed with the three acquisitions. In the Poor BH case, substantial motion artifact is observed in the BH 3D acquisition. In contrast, the free-breathing 2D acquisitions (LFA-linear and VFA-centric) effectively freeze breathing motion. In both subjects, LFA-linear acquisition leads to high noise levels in PDFF maps. The proposed VFA-centric method is able to freeze breathing motion while maintaining high SNR. Yellow circles represent sample ROIs used for further analysis.
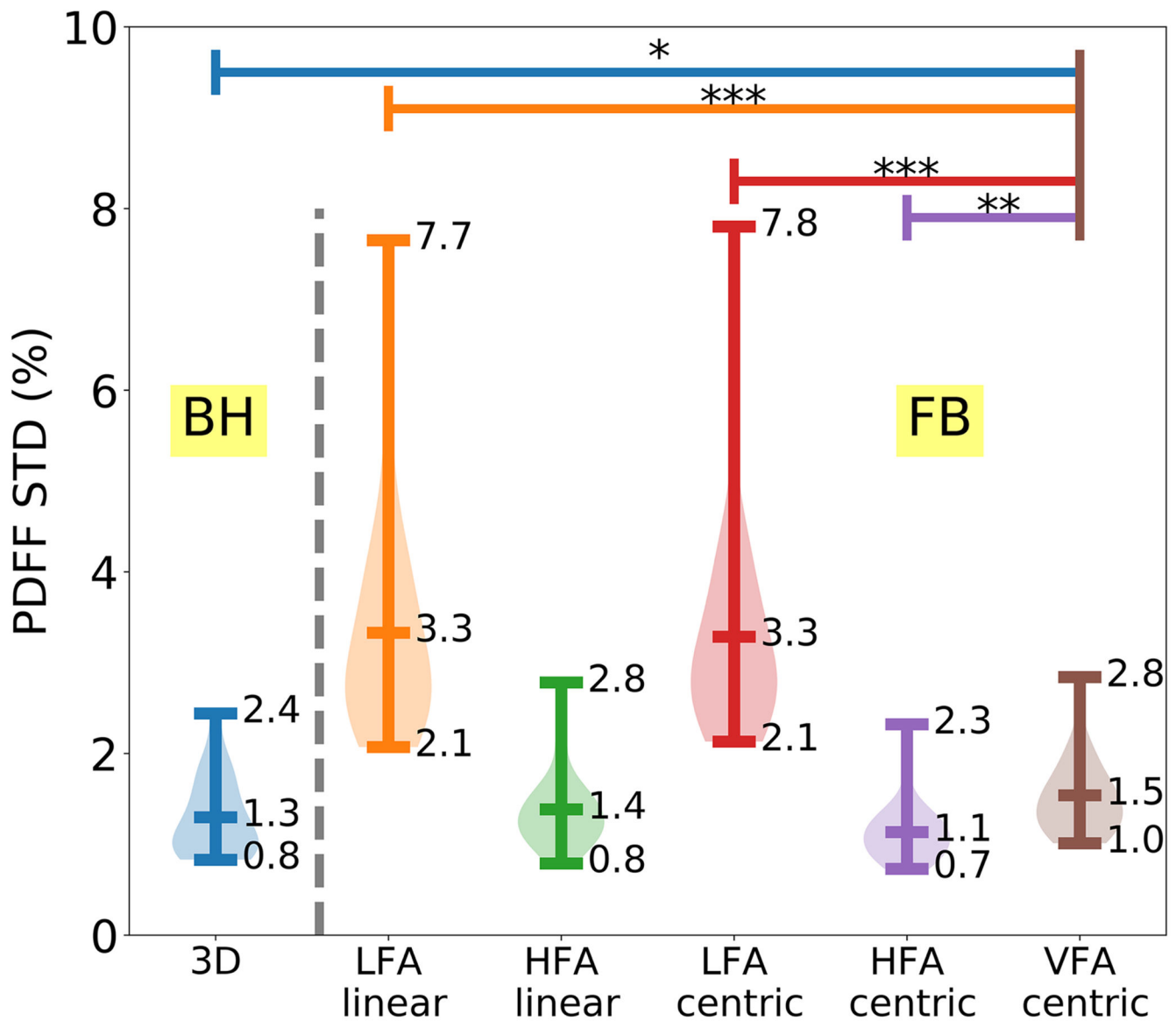
Figure 5.
Representative PDFF maps from three adults with increasing fat fraction level using three different CSE-MRI acquisitions (3D, LFA-linear, and VFA-centric). All three acquisitions show good agreement in liver fat quantifcation. BH 3D acquisition requires breath-hold during scanning, whereas the 2D acquisitions (LFA-linear and VFA-centric) are acquired during free-breathing. The proposed VFA-centric acquisition leads to visually apparent improved noise performance compared to the standard LFA-linear acquisition. Yellow or black circles represent sample ROIs used for further analysis.

Figure 6.
Linear regression (top row) and Bland-Altman analysis (bottom row) between measured PDFF from five different CSE-MRI acquisitions (3D, HFA-linear, LFA-centric, HFA-centric, and VFA-centric) and reference PDFF (LFA-linear) across all subjects in this study. High correlation in PDFF measurements is observed between the reference LFA-linear acquisition and each of the five additional acquisitions. Based on Bland-Altman plots, the proposed VFA-centric method provides close agreement with low bias and narrow limits of agreement in PDFF measurement (Bias = 0.0%, 95 % LoA = −0.5% to 0.6%), compared to the reference LFA-linear acquisition.

Figure 7.
The proposed VFA-centric method enables liver PDFF mapping with high SNR performance (i.e., low standard deviation in PDFF measurement). Plot shows ROI-based PDFF standard deviation measurements across all subjects between six different CSE-MRI acquisitions (3D, LFA-linear, HFA-linear, LFA-centric, HFA-centric, and VFA-centric). The proposed VFA-centric method has relatively low mean standard deviation of 1.5%, comparable to HFA acquisitions and lower than LFA acquisitions. From the Bonferroni corrected t-test results, the proposed VFA-centric method shows highly significant difference (lower standard deviation) with LFA-linear acquisition (p <0.001) and LFA-centric acquisition (p <0.001). Further, the VFA-centric acquisition shows significant difference (higher standard deviation) with HFA-centric acquisition (p = 0.006) and no statistically significant difference with HFA-linear acquisition (p = 0.2). (* p<0.05, • ** p<0.01, *** p<0.001)

TABLE 1

Details regarding five 2D Cartesian sequential CSE-MRI acquisitions.

Acquisition	Flip Angle Schedule	Phase Encoding Method	Discarded TRs
LFA-linear	Constant 3°	linear	4
HFA-linear	Constant 15°	linear	4
LFA-centric	Constant 3°	centric	0
HFA-centric	Constant 15°	centric	0
VFA-centric	Variable Flip Angle	centric	0

TABLE 2

Spectroscopy measured T_1 values for each vial in the phantom.

Nominal PDFF	0%	10%	20%	30%	40%
Target $T_{1,water}$=300 ms [CuSO$_4$ (4.0 mM)]	321 ms	331 ms	337 ms	343 ms	349 ms
Target $T_{1,water}$=600 ms [CuSO$_4$ (2.0 mM)]	560 ms	609 ms	617 ms	620 ms	625 ms
Target $T_{1,water}$=900 ms [CuSO$_4$ (2.0 mM)]	934 ms	992 ms	943 ms	1007 ms	1010 ms
Target $T_{1,water}$=1200 ms [CuSO$_4$ (0.5 mM)]	1216 ms	1205 ms	1205 ms	1208 ms	1208 ms

$T_{1,fat}$ measurements in the vials with PDFF >0% were within 350± 12 ms.

TABLE 3

Linear mixed-effects model analysis of PDFF bias for five different 2D Cartesian sequential CSE-MRI acquisitions.

	LFA-linear	HFA-linear	LFA-centric	HFA-centric	VFA-centric
Intercept	0.02±0.71 p = 1.00	−0.75±0.88 p = 0.39	0.15±0.71 p = 0.83	0.12±0.68 p = 0.86	0.21±0.71 p = 0.77
true PDFF	−0.05±0.03 p = 0.10	−0.17±0.04 ** p < 0.01	−0.04 ±0.03 p = 0.14	−0.09 ±0.03 ** p < 0.01	−0.06±0.03 p = 0.05
$T_{1,water}$ (×10⁻³)	0.80±0.83 p = 0.34	2.47±1.04 * p = 0.02	0.66±0.83 p = 0.43	1.10±0.80 p = 0.17	0.56±0.83 p = 0.50
true PDFF· $T_{1,water}$ (×10⁻³)	0.06±0.03 p = 0.09	0.30±0.04 ** p < 0.01	0.04 ±0.03 p = 0.23	0.07±0.03 * p = 0.04	0.06±0.03 p = 0.09

*
$p<0.05$

**
$p<0.01$.